Journal of Applied Fluid Mechanics, Vol. 16, No. 12, pp. 2540-2555, 2023.
Available online at www.jafmonline.net, ISSN 1735-3572, EISSN 1735-3645.
https://doi.org/10.47176/jafm.16.12.1875

Temporal Flow Characteristics of Three-Dimensional Centrifugal Impeller Suction System at Vacuum Conditions

Y. Li[1], B. Zhang[2], Y. Chen[1], Z. Wang[1], H. Yang[1] and Y. Wei[1†]

[1]*Key Laboratory of Fluid Transmission Technology of Zhejiang Province, Zhejiang Sci-Tech University, Hangzhou, Zhejiang 310018, China*
[2]*Denair Energy Equipment Co., Ltd*

†*Corresponding Author Email: yikunwei@zstu.edu.cn*

ABSTRACT

Temporal flow characteristics of a 3D centrifugal impeller suction system were numerically studied in vacuum conditions. The blockage of the high-speed rotating impeller appeared, which greatly dropped the suction of the layer suction device. The temporal flow characteristics of the 3D centrifugal impeller suction system were worthy of attention in vacuum conditions. Separation vortices were generated near the blade suction surface. The blocking mechanism of the passage was further analyzed at different extremely low flow rates through the time-space evolution of the streamline. The Q-criteria was introduced to analyze the vortex evolution within the fluid domain of the impeller. Vortex evolution law was captured—the vortices always generated near the suction surface of the blade and moved to the pressure surface of the adjacent blade in the same passage and disappeared. The uniform distribution of three stall cells was captured through the diagram of turbulent kinetic energy. The flow rate increased, and the vortex evolution period gradually decreased. The comparison of pressure fluctuations in different conditions further demonstrated the flow mechanism at the vacuum flow rate was different from that at low flow rates. The sharp increase of pressure fluctuations near the blade pressure surface was consistent with the phenomenon near the suction surface. The pressure fluctuation at extremely low flow was mainly composed of scattered fluctuations caused by fluid separation. The steady and unsteady characteristics described the internal flow characteristics of this suction system at vacuum-flow rates. Theresults provide a profound design for vacuum cleaners.

Article History

Received March 22, 2023
Revised July 26, 2023
Accepted August 2, 2023
Available online October 8, 2023

Keywords:

Centrifugal blower
Fluid structure
Pressure fluctuation
Spectrum analysis
Time evolution characteristics

1. INTRODUCTION

The vacuum cleaner is a common household appliance in our daily life. The impeller is the key rotating part of the vacuum system in the vacuum cleaner. The vacuum degree represents one of the key indices for the impeller of the vacuum cleaner. The performance of the impeller depends on the complex internal flow structure within the impeller. Besides, the performance of the impeller determines the efficiency of the vacuum cleaner. Therefore, the improvement of the centrifugal blower is critical to improving the vacuum cleaner and reducing energy consumption. The centrifugal blower used for vacuum cleaners usually works at a low flow rate to achieve a high vacuum degree. However, the internal flow of the centrifugal impeller is extremely complex in vacuum conditions. The whole impeller is blocked seriously by a large number of separation vortices in the impeller, which drastically increases the aerodynamic noise of the impeller and severely damages the impeller.

The prediction of stall has been widely studied. Zhang et al. (2020) reviewed the recent research on the rotating stall of the centrifugal compressor and emphatically introduced the inductive mechanism and characteristic description of rotating stall. As described by Ghenaiet and Smail (2019), the determination of stall onset is important for the control and safety of centrifugal compressors, and the quantification of the blockage factor is more suitable for predicting the stall onset and stall cell positions. Zhang et al. (2021a)

NOMENCLATURE

D	diameter	T	temperature
E	internal energy	t	time
F	inertia force	v	velocity
G	turbulent kinetic energy	α	angle
H	enthalpy	β	expansion coefficient
h	height	ρ	fluid density
k	heat transfer coefficient	μ	viscosity
P	pressure		

investigated the development process of stall as well as the sensitive locations of centrifugal compressors with vaneless diffusers and volute. Besides, two development stages of stall in the centrifugal compressor are summarized, which provides profound insights for the subsequent study on the stall phenomena. Yuki et al. (2022) studied the rotating stall through numerical and experimental methods. Boundary layer separation near the impeller outlet plays an important role in the expansion processes of stall. Experimental and numerical methods are always used to study the stall mechanism in centrifugal pumps (Liu et al., 2022). Xue and Wang (2019) proposed an index capable of identifying the severity at varying speeds, which prevents surge and deep stall during practical compressor operating. The index can define stall's enormity and prevent deep stall or surge. Niu et al. (2022) explored the effect of volute on rotating stall through experiments and numerical simulations. Stall is closely related to circumferentially non axisymmetric pressure distribution due to volute. It can be weakened or suppressed by optimizing the geometry of volute. Semlitsch et al. (2016) analyzed the flow evolution of centrifugal compressors through the3D unsteady simulation of centrifugal compressors. The design condition is compared with the low flow condition with surge. Their studies intuitively demonstrate the flow structure under the design condition and the near surge conditions. Studying the surge mode is significant. Mischo et al. (2018) combined the numerical method and experiment to verify the stability of the unshroud centrifugal compressor with a high rotating speed. The unsteady interaction between rotating stall unit and the crown-free centrifugal compression stage is reproduced in two different full-scale compression units.

A 3Dblade can improve impellers. The complex 3D modeling of centrifugal compressor blades is mainly determined by middle arc-angle distribution, sweep feature, and lean feature. The shock wave and flow separation in the impeller are significantly influenced by the distribution of the leading angle of the blade's middle arc. Li et al. (2018) argued that reducing the leading-edge curvature of the middle arc of the blade tip section can reduce the Mach number of shock wave fronts and corresponding flow losses. The swept characteristic is one of the freedom degrees that determines the stacking law of blades. The swept blade has been extensively studied in axial compressor rotors (Vad 2008). Moreover, the lean characteristic is an important freedom degree of blade-stacking law. He and Zheng (2016) found that the lean characteristic has the potential to control the shock wave geometry and suppress the generation of wake. The performance of the compressor is influenced by the blade lean (Cao et al., 2022). Du et al. (2020) adopted an impeller with 3D blades to research rotating stall and illustrated the propagation mechanism of stall cells in the centrifugal compressor. Zhang et al. (2021b) illustrated the stall mechanism in an ultra-high-pressure-ratio centrifugal compressor. The compressor model with3D blades is used for unsteady numerical simulations that trace the onset of instability in the compressor. Chen et al. (2023) studied the time-space characteristics of a high-speed centrifugal blower with 2D blades at low flow.

The previous study of centrifugal blowers used for vacuum cleaners mainly focuses on the noise reduction and optimization of centrifugal blowers. Jeon et al. (2003) introduced a method to calculate the unsteady flow fields and aeroacoustic sound pressure in the centrifugal fan of a vacuum cleaner. An et al. (2022) committed to reducing the noise of using vacuum cleaners in the desired frequency band. Soheil (2022) used the optimization technique based on asurrogate. They focused on maximizing the Airwatt parameter and minimizing shaft power to reduce vacuum cleaner power consumption. The centrifugal blower used for vacuum cleaners always works at high speeds and a low flow rate due to the pursuit of a high vacuum degree. It is easy to bring the blockage of the high-speed rotating impeller in vacuum, which greatly drops the suction of the layer suction device. The spatio-temporal characteristics of the3D centrifugal-impeller suction system are worthy of attention in vacuum conditions.

Based on the above discussions, the work considered the aerodynamic performance of the centrifugal blower in vacuum conditions (at extremely low flow rates). The blockage mechanism and the internal flow evolution of the centrifugal blower are discussed in vacuum condition with an emphasis on the time-space evolution characteristics of internal complex flow mechanisms. The pressure fluctuation is also thoroughly discussed. The governing equations and numerical models are briefly described in Section 2. Section 3 presents the steady and unsteady numerical results and some discoveries of numerical simulations in vacuum conditions. Some constructive conclusions are summarized in Section 4.

2. GOVERNING EQUATIONS AND NUMERICAL METHOD

2.1 Governing Equations of Fluid Flow

Centrifugal blowers involve a rotating coordinate

system, and the frozen rotor method is the main way to deal with this problem. The basic governing equations (Wang et al., 2020; Wei et al., 2020) that denote the mathematical description of the physical law of the fluid mechanism are expressed as follows.

The continuity equation is

$$\frac{\partial \rho}{\partial t}+\frac{1}{r}\left[\frac{\partial\left(\rho v_r r\right)}{\partial r}+\frac{\partial\left(\rho v_\theta\right)}{\partial \theta}+\frac{\partial\left(\rho v_z r\right)}{\partial z}\right]=0 \tag{1}$$

The momentum conservation equation is

$$\rho\left(\frac{dv_r}{dt}-\frac{v_\theta^2}{r}\right)=\rho F_{br}+\frac{1}{r}\left[\frac{\partial\left(p_{rr} r\right)}{\partial r}+\frac{\partial\left(p_{r\theta}\right)}{\partial \theta}+\frac{\partial\left(p_{rz} r\right)}{\partial z}-p_{\theta\theta}\right] \tag{2}$$

$$\rho\left(\frac{dv_\theta}{dt}+\frac{v_r v_\theta}{r}\right)=\rho F_{b\theta}+\frac{1}{r}\left[\frac{\partial\left(p_{r\theta} r\right)}{\partial r}+\frac{\partial\left(p_{\theta\theta}\right)}{\partial \theta}+\frac{\partial\left(p_{\theta z} r\right)}{\partial z}+p_{r\theta}\right] \tag{3}$$

$$\rho\frac{dv_z}{dt}=\rho F_{bz}+\frac{1}{r}\left[\frac{\partial\left(p_{rz} r\right)}{\partial r}+\frac{\partial\left(p_{\theta z}\right)}{\partial \theta}+\frac{\partial\left(p_{zz} r\right)}{\partial z}\right] \tag{4}$$

where ρ is the density; t is time; p is the pressure; v_r, v_θ and v_z are velocities in different directions, respectively.

The total energy equation is

$$\rho\frac{dH}{dt}=\frac{1}{r}\left[\frac{\partial}{\partial r}\left(rk\frac{\partial T}{\partial r}\right)+\frac{\partial}{\partial \theta}\left(\frac{k}{r}\frac{\partial T}{\partial \theta}\right)+\frac{\partial}{\partial z}\left(rk\frac{\partial T}{\partial z}\right)\right]+\rho q+\frac{dp}{dt}+\varphi \tag{5}$$

where *k*isthe heat transfer coefficient of the fluid medium.

2.2 Turbulence Model

The k-epsilon turbulence model is extensively applied to study steady flow. This turbulence model incorporates the concepts of turbulence kinetic energy and turbulence dissipation rate. It also links the turbulent viscosity coefficient and fluctuation kinetic energy to the characteristic scale of fluctuations (Wolfram et al., 2010). The standard k-epsilon model can be expressed by the following equations.

$$\rho\frac{Dk}{Dt}=\frac{\partial}{\partial x_i}\left[\left(\mu+\frac{\mu_t}{\sigma_k}\right)\frac{\partial k}{\partial x_i}\right]+G_k+G_b-\rho\varepsilon \tag{6}$$

$$\rho\frac{D\varepsilon}{Dt}=\frac{\partial}{\partial x_i}\left[\left(\mu+\frac{\mu_t}{\sigma_\varepsilon}\right)\frac{\partial \varepsilon}{\partial x_i}\right]+C_{1\varepsilon}\frac{\varepsilon}{k}\left(G_k+G_{3\varepsilon}G_b\right)-C_{2\varepsilon}\rho\frac{\varepsilon^2}{k} \tag{7}$$

where μ_t is the turbulent viscosity coefficient ($\mu_t=\rho C_\mu\frac{k^2}{\varepsilon}$); C_μ is the turbulent constant; G_k is the generation of turbulent kinetic energy from average velocity gradient ($G_k=\mu_t\left(\frac{\partial u_i}{\partial x_j}+\frac{\partial u_j}{\partial x_i}\right)\frac{\partial u_j}{\partial x_j}$); G_b is the generation of turbulent kinetic energy caused by buoyancy. $G_b=\beta g_i\frac{\mu_t}{\mathrm{Pr}_r}\frac{\partial T}{\partial x_i}$, where β is the expansion coefficient ($\beta=-\frac{1}{\rho}\frac{\partial \rho}{\partial T}$).

The LES (large eddy simulation) used to study the unsteady simulation can capture the comprehensive characteristics of turbulent flow (Borello et al., 2013). As the control equation of the LES simulation, the Navier-Stokes equation is presented.

$$\frac{\partial \rho}{\partial t}+u\frac{\partial \rho\overline{u_i}}{\partial x_i}=0 \tag{8}$$

$$\frac{\partial}{\partial t}\left(\rho\overline{u_i}\right)+\frac{\partial}{\partial x_j}\left(\rho\overline{u_i u_j}\right)=\frac{\partial}{\partial x_j}\left(\mu\frac{\partial \overline{u_i}}{\partial x_j}\right)-\frac{\partial \overline{P}}{\partial x_j}-\frac{\partial \tau_{ij}}{\partial x_j} \tag{9}$$

where $\tau_{ij}=\rho\overline{u_i u_j}-\rho\overline{u_i}\cdot\overline{u_j}$ is sub-grid stress.

2.3 Simulation Setting

Software ANSYS CFX19.2 was used in all numerical simulations. The boundary conditions of the computational domain were set as follows:

-The total pressure and temperature were 101,325 Pa and 288.15 K in the inlet boundary condition, and the static pressure was chosen as the outlet boundary condition. The flow rate was changed by controlling the pressure at the outlet.

-The ideal gas was selected as the medium of the simulation, and the reference pressure was 0 Pa.

-The mass and momentum boundary condition was set as a no-slip wall, and the heat transfer was selected as the adiabatic boundary condition.

-The connection mode of the interface connected with the impeller was set as a general connection, and the frame change mode was chosen as the frozen rotor method.

-The standard k-ε turbulence model was implemented for a steady simulation.

-The LES turbulence model was used for an unsteady simulation. Time step independence was verified in the designed operating condition. The pressure ratio of the blower was almost not affected when the time step was less than 4.76×10-6s. For each working condition, 20 rotation periods were performed, and the stable state of the last revolution was implemented to capture the spatio-temporal characteristics of the 3D centrifugal impeller.

3 Model Setting and CFD Study

3.1 Geometry Model of the Suction System

Table 1 lists the main parameters of the centrifugal blower. All computational domains are created by SolidWorks and blade Gen. The centrifugal blower is composed of an impeller with a 3D blade and flow diverter (Fig. 1(a)). The flow wake loss at the outlet of the high-speed impeller is relatively high. The flow diverter with nine blades is implemented to reduce the flow loss at the impeller outlet. Figure 1(b) presents the structure characteristics of the blade for the flow diverter. Figure 1(c) shows the 3D model of the centrifugal blower. The light grey part represents the impeller; the blue part

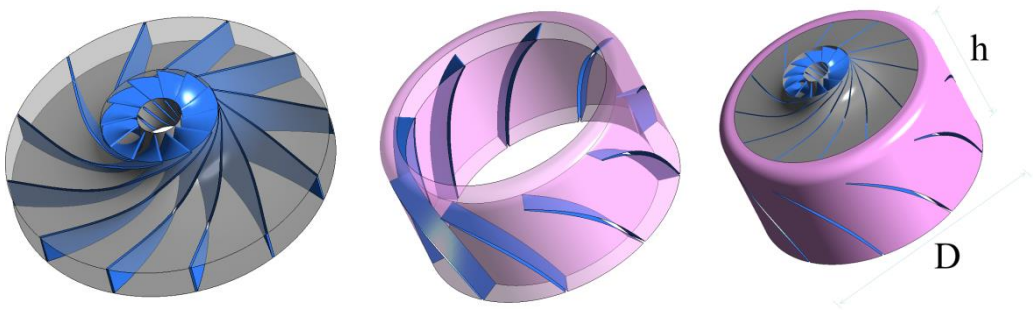

(a) (b) (c)

Fig. 1 Geometry of the centrifugal blower

Table 1 Main parameters of the centrifugal blower

Parameter	Unit	Value
Compressor		
Design rotational speed	rpm	70000
Impeller		
Inlet hub diameter	mm	6
Inlet shroud diameter	mm	16
Outlet diameter	mm	44
Outlet width	mm	5
Number of blades	—	12
Blade back-sweep angle	degree	67
Flow diverter		
Height (h)	mm	28.5
Diameter (D)	mm	53
Inlet width	mm	5
Outlet width	mm	4.5
Number of blades	—	9

represents the blade; the pink part corresponds to the flow diverter. Besides the flow diverter diameter and height are specified. In general, the 3D blade is to reduce vortex generation. Thus, the 3D impeller is implemented for energy conservation in the work.

The rotating speed of the impeller is 70,000rpm, and the blade back-sweep angle is 67°.

3.2 Grid system of the Suction System

Figure 2 exhibits the whole grid schematic and some details of the grid. Each part of the centrifugal blower system composed of hexahedral structural meshes can obtain relatively accurate numerical results. The impeller inlet and the flow diverter outlet are extended to build a complete computational domain based on the original structure (Fig. 2 (a)). The black part at the top of the model is the impeller-inlet extension, and the dark grey part at the bottom of this model is the extension of the flow diverter outlet. Figure 2(b) presents the grid diagram at the leading edge and trailing edge areas of the blade. Therefore, the dense grid near the leading edge and trailing edge of the blade can be observed more limpidly. Figure 2(c) shows the detail of the grid near the flow diverter blade. As shown in the enlarged part of the red box of Fig. 2, the mesh of the blade boundary layer is encrypted to capture the flow field information of fine separation in the blade boundary layer, which improves the accuracy of the numerical simulation.

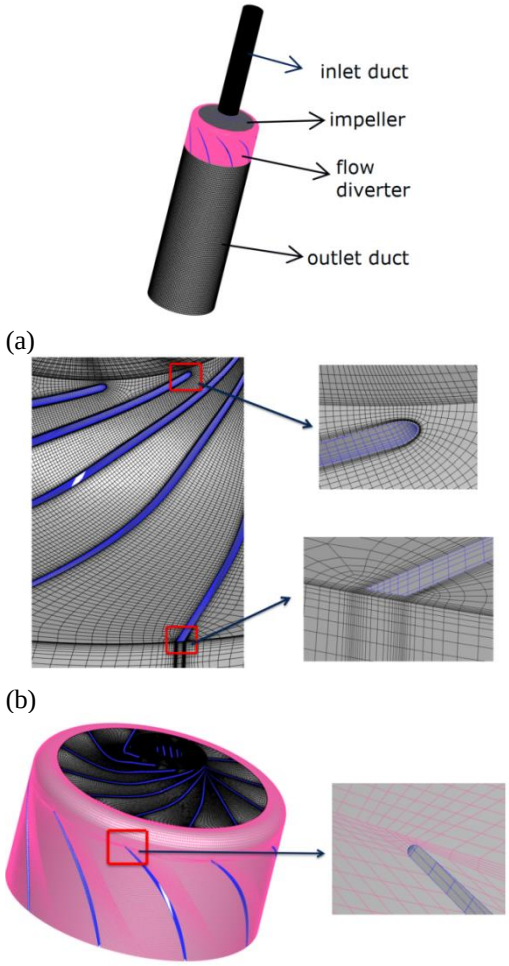

(a)

(b)

(c)

Fig. 2 Grid structure of (a) whole frame, (b) centrifugal blower, and (c) flow diverter

3.3 Verification of Mesh Independence

The accuracy of the numerical simulation is affected by the mesh quality and the number of grids. The validation of grid independence is necessary. Figure 3 displays the vacuum-degree comparison of six sets of grids with different grid number. The vacuum degree of the centrifugal blower is closely related to grid number in Fig. 3. The influence of grid number is significant when the number of nodes in the grid is less than 2.7 million. When grid number increases from 2.7 million to 3.6 and 5.01 million, the vacuum degree is decreased by 0.19 and 0.47%, respectively. That is, the effect of grid number

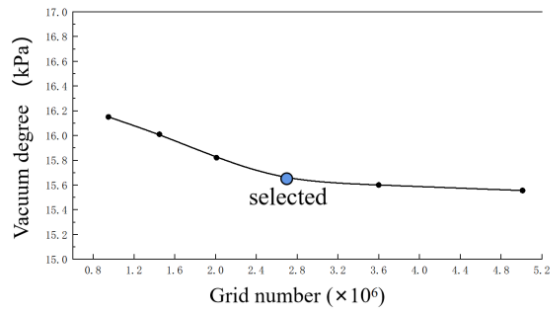

Fig. 3 Pressure ratios for different number of nodes

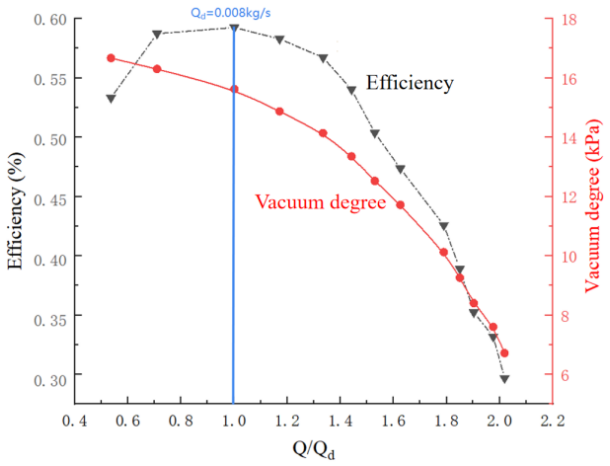

Fig. 4 Performance curve of the system

can be neglected when grid number exceeds 2.7 million. Thus, the grid with 2.7 million nodes is chosen for the subsequent numerical simulation.

3.4 External characteristic parameters of the centrifugal blower

Figure 4 describes the curve of efficiency and pressure ratio of this centrifugal blower at different flow rates. The black curve of efficiency shows that the optimal efficiency point occurs at the flow of 0.008kg/s, which is chosen as the design condition. The efficiency drops rapidly with the decreased flow rate of less than $0.7Q_d$. Relatively high efficiency can be remained by this centrifugal blower in a range of $0.7\text{-}1.4Q_d$. As shown from the red B-spline curve, the vacuum degree gradually decreases with the increased flow rate. A large vacuum degree can be preserved by this centrifugal blower when the flow rate is close to Q_d. The vacuum degree is the main objective of this simulation due to the application field of this centrifugal blower in the work. Therefore, 0.008kg/s is selected as the design condition for this simulation by considering the high-efficiency area of the centrifugal blower and comparing the flow mechanism under different flow rates.

Table 2 summarizes the external parameters of the centrifugal blower in design conditions. The inlet pressure is taken from the inlet terminal of the inlet extension. Similarly, the outlet pressure is taken from the outlet terminal of the outlet extension. The pressure difference between these two endpoints reaches 15.63kPa, that is, the vacuum degree is 15.63kPa.

Table 2 Parameters of the blower in the design condition

Item	Unit	Value
Inlet pressure	kPa	100.67
Outlet pressure	kPa	116.30
Vacuum degree	kPa	15.63
Pressure ratio	—	1.16
Mass flow rate	kg·s-1	0.008
Efficiency	%	59

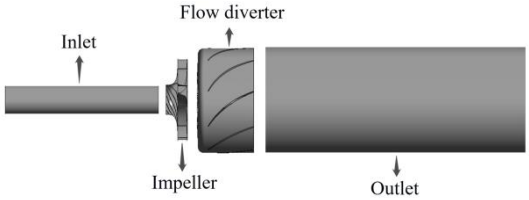

Fig. 5 Computational domain

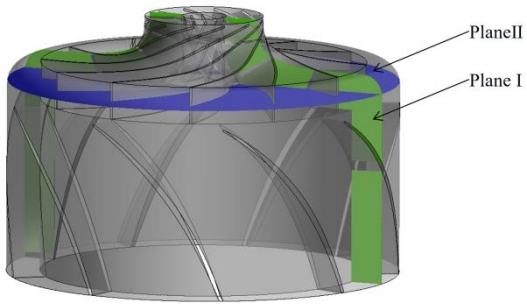

Fig. 6 Location of Planes I and II

3.5 Steady Internal-Flow Analysis of the Suction System

The centrifugal blower is mainly divided into the centrifugal impeller, the flow diverter, and the computational domain of the inlet and outlet in all numerical simulations, respectively. The impeller has twelve blades, and the volute is replaced by the flow diverter to be more suitable for vacuum cleaners in the work. The flow diverter has nine static blades and plays a good diversion role, which reduces energy consumption. The impeller outlet is directly connected to the flow diverter inlet. Every part of the computational domain is shown separately (Fig. 5).

Figure 6 shows the location of Planes I and II. The impeller and flow diverter is translucent to illustrate the position of Planes I and II more intuitively. Plane I is the green area indicated by the arrow in Fig. 6. The qualitative analysis on Plane I can contribute to easily understanding the axial distribution of the aerodynamic characteristics of the centrifugal blower. The blue plane specified by the arrow represents Plane II, which can favor comprehending the radial distribution of the flow mechanism.

Figure 7 presents the distribution of total pressure and temperature in Plane I for displaying the distribution of aerodynamic characteristics in the axial direction.

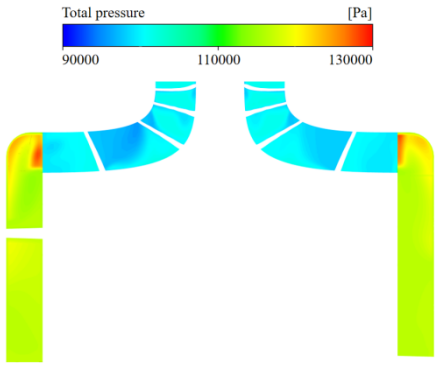

(a) Total pressure

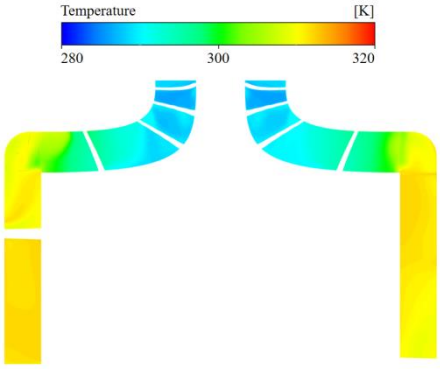

(b) Temperature

Fig. 7 Distributions of the total pressure and temperature at plane I

Figure 7(a)shows the axial distribution of total pressure, and the gradual increase of total pressure is relatively uniform along the flow passage of the impeller. However, the total pressure increases near the flow diverter inlet. The fluid with a relatively high speed due to the high-speed blade is blocked. The temperature distribution shows the raised temperature in the axial direction is smoother than the total pressure (Fig. 7 (b)). The temperature gradually increases along the passage because of the flow separation and viscosity loss of the boundary layer as well as a part of fluid kinetic energy converted into thermal energy. However, there is almost no soar in temperature, indicating that the design is reasonable with high security.

Figure 8 depicts the distribution of streamline in Plane II in different conditions. The impeller rotates in a counterclockwise direction. These three different conditions show that the blockage is relieved with the increased flow rate. The block mainly occurs near the suction surface of the blade, and the fluid flows out of the impeller near the blade pressure surface. Besides, the discharge from the impeller has a high speed due to the high-speed impeller. Fluid blockage is serious at a flow rate of $0.7Q_d$ and almost occupies the whole passage (Fig. 8 (a)). A periodicity exists in the generation, development, and disappearance of the back-flow vortices.

The vortex area in different passages is gradually expanded along the rotating direction and then disappears after reaching the peak. This phenomenon is particularly evident at Q_d (Fig. 8 (b)). The vortex in the marked channel gradually expands along the arrow direction (rotating direction) and reaches the maximum in the last channel included by the red marking circle. The vortex evolution within the channel outside the red circle illustrates the process of vortex reduction. The evolution of the vortex in the flow passages within the next red marking circle show the development of vortex again. Three marking frames indicate three periods of vortex development in a rotating cycle in the design condition. Fig. 8(c) represents the streamline in Plane II at 1.4 Q_d. Blockage evolution law mentioned above is not obvious at $1.4Q_d$ with the increased flow rate. However, the blockage of blade passages has been significantly relieved at 1.4 Q_d compared with the design conditions.

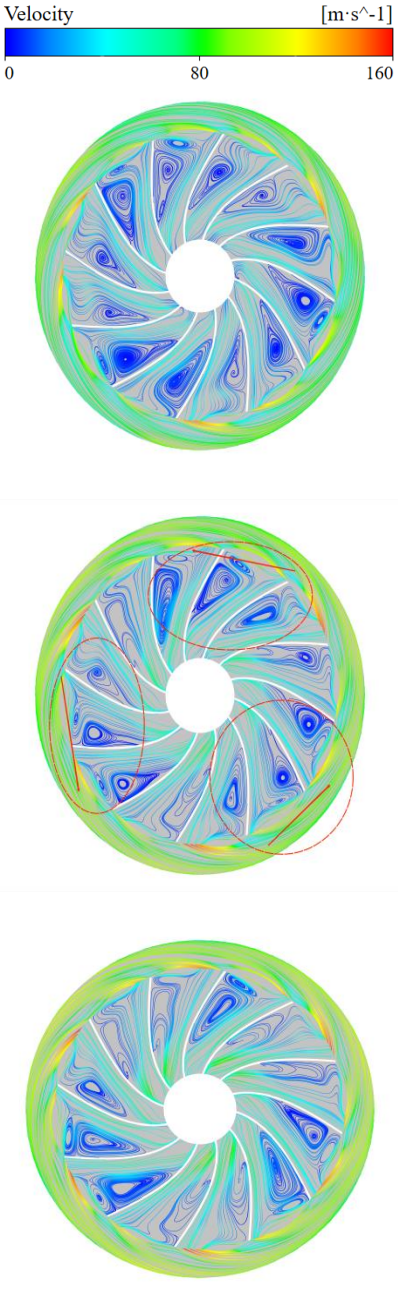

(a)

(b)

(c)

Fig. 8 Distribution of streamline at Plane II(a) $0.7Q_d$, (b) Q_d, and (c) $1.4Q_d$

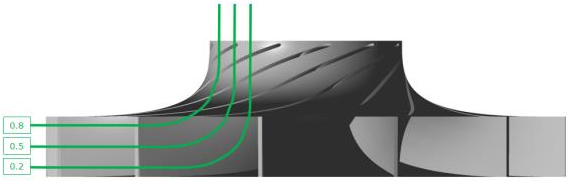

Fig. 9 Locations of different spans

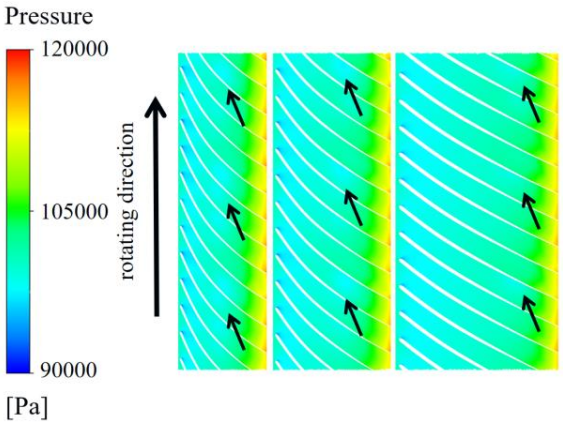

(a) (b) (c)

Fig. 10 Distributions of static pressure at(a) 0.2 span, (b) 0.5 span, and (c) 0.8 span

Figure 9 demonstrates the locations of different spans. The dark grey part represents the impeller, and the green curve represents the profile of the span surface. We select0.2, 0.5, and 0.8 spans to stereoscopically display flow inside the impeller.

Figure 10 shows the pressure distribution in the passage outspread diagram. The lowest pressure mainly occurs near the leading edge of the blade pressure surface. The pressure gradient within the passage gradually increases. This phenomenon is well consistent with total-pressure variable law (Fig. 7 (a)). Besides, three low-pressure regions are remarked in each span, and the distribution of these low-pressure regions is particularly regular. The appearance of these low-pressure areas is caused by the movement of the vortex in the passage. Three low-pressure areas exist in the rotating period of the impeller, which coincides with the motion law of the vortices (Fig. 8). These low-pressure vortices constantly appear, disappear, and transfer in various impeller passages, which results in numerous unstable effects on the impeller. The motion law of these low-pressure areas is studied to better understand the flow mechanism inside the impeller and extend the service life of the centrifugal blower. The impeller outlet is covered by the high-pressure region. There is almost no fluid flowing out and the flow structure is blocked, which results in the stall phenomenon.

Figure 11 describes the 3D streamline in the flow diverter. The flow diverter is used to change the flow direction of high-speed fluids at the impeller outlet and plays the role of pressure expansion. It significantly affects the whole centrifugal compressor. Fluids first flow at high speeds at the top of the flow diverter. Then they change the flow direction under the smooth curve surface and flow out of the flow diverter along the blade

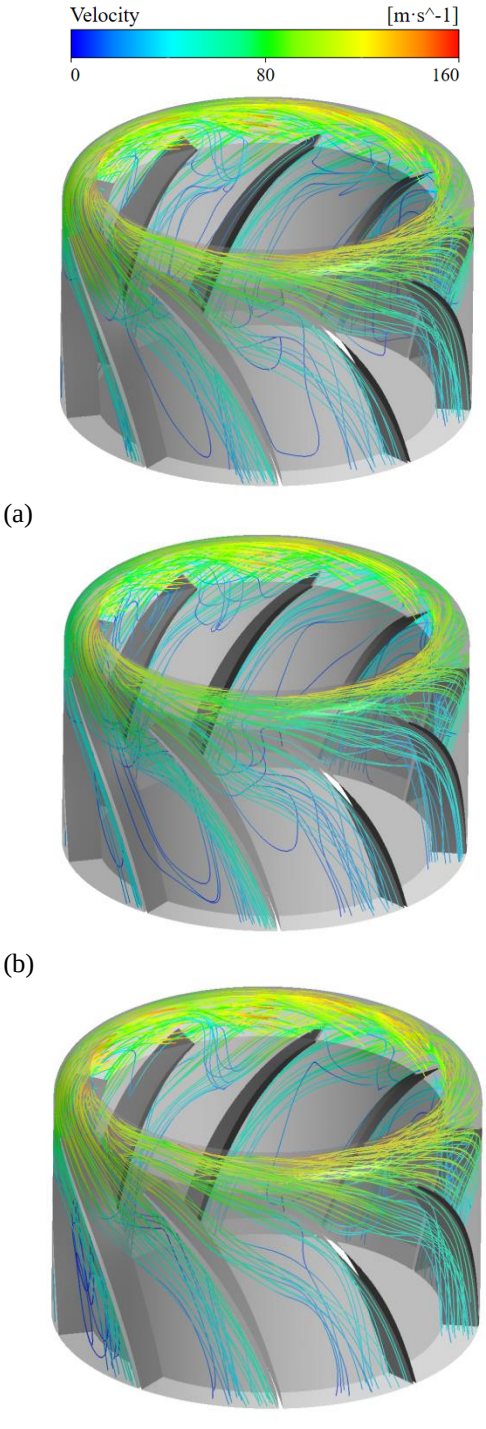

(a)

(b)

(c)

Fig. 11 Distribution of streamline in the flow diverter at (a) 0.7Q_d, (b) Q_d, and (c) 1.4Q_d

pressure surface (Fig. 11 (a)). Some low-pressure areas appear near the suction surface of the diverter blade, and back-flow is captured. Refluxes can still be detected in each flow diverter passage (Fig. 11 (b)). When the flow rate increases to 1.4 Q_d, backflow is significantly ameliorated.

Turbulent kinetic energy (TKE) is widely used to measure turbulent fluctuations, which is positively correlated with velocity fluctuations. Thus, it is reflected in the energy dissipation in the flow region, and the high

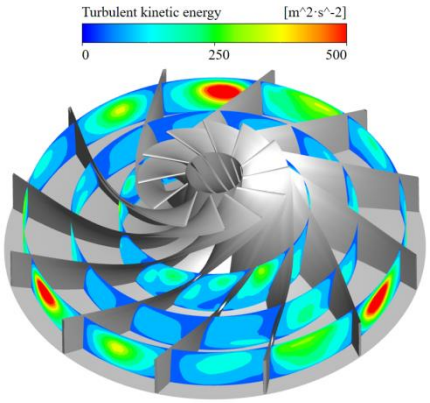

Fig. 12 Circumferential distributions of turbulent kinetic energy along the flow passage

TKE value represents the high flow loss (Dang et al., 2019). The numerical expression for TKE is as follows:

$$\mathrm{TKE}=\frac{3}{2}(vI)^2 \tag{10}$$

where v is velocity; I is the intensity of turbulent flow.

Figure 12 illustrates the distribution of TKE on the three annular sections in the design condition. These circumferential surfaces are located at the middle, end, and outlet of the passage. As exhibited by the outermost section, three regions with high TKE are uniformly distributed. High TKE regions are always near the blade pressure surface, indicating that the pressure fluctuation is more severe near the pressure surface. Besides, the changing trends of TKE show significant periodicity along the rotational direction. TKE exhibits a pattern of peaking, gradual decline, and subsequent resurgence after traversing two passages to reach the next peak. The surface has lower TKE near the center. Energy dissipation mainly occurs near the impeller outlet. The distribution of turbulent kinetic energy illustrates the dissipation of energy within the impeller and provides precise elaboration on the fluid structure. It is helpful for us to understand the flow mechanism of the high-speed centrifugal suction system operating at an extremely low flow rate.

3.6 Streamlines and flow structures of the centrifugal blower

Figure 13 shows the spatio-temporal evolution of streamline in the impeller passage of a rotating period in different operating conditions. Figure 13(a)shows the impeller-rotating direction at time $t=t_0$ All of the instantaneous streamlines are captured from a 0.2 span (Fig. 9). As mentioned above, flow conditions are intentionally reduced to enhance the vacuum degree; therefore, serious blockages can be observed in the flow passage. Ten channels are marked in each streamline diagram to study the space-time evolution of the streamline.

Figure 13 (a) represents the streamline at $0.7Q_d$. An obvious vortex blocks channel 4 at $t = t_0$. The blockage in channel 4 starts to separate at $t = t_0 + 1/4T_1$. When $1/2T_1$ is turned, the blockage gradually separates into two vortices.

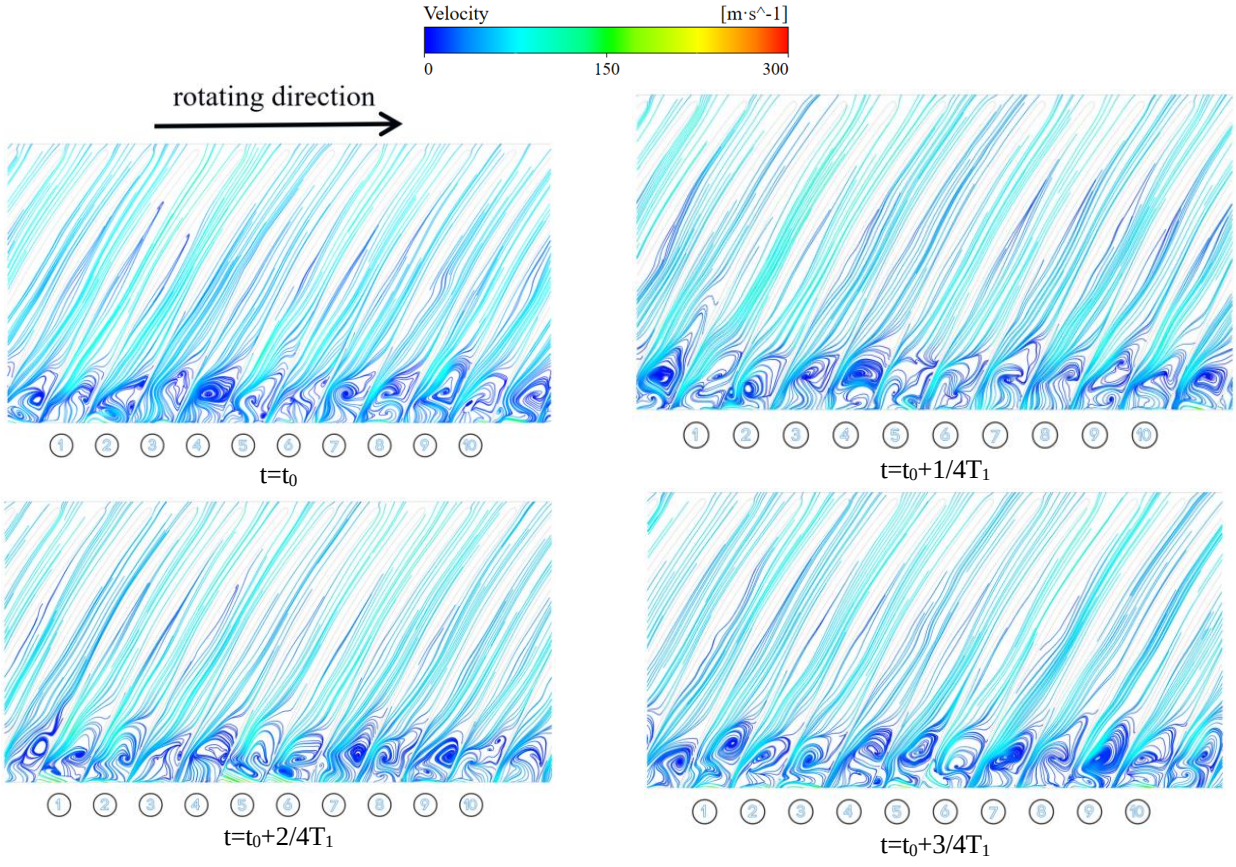

(a)

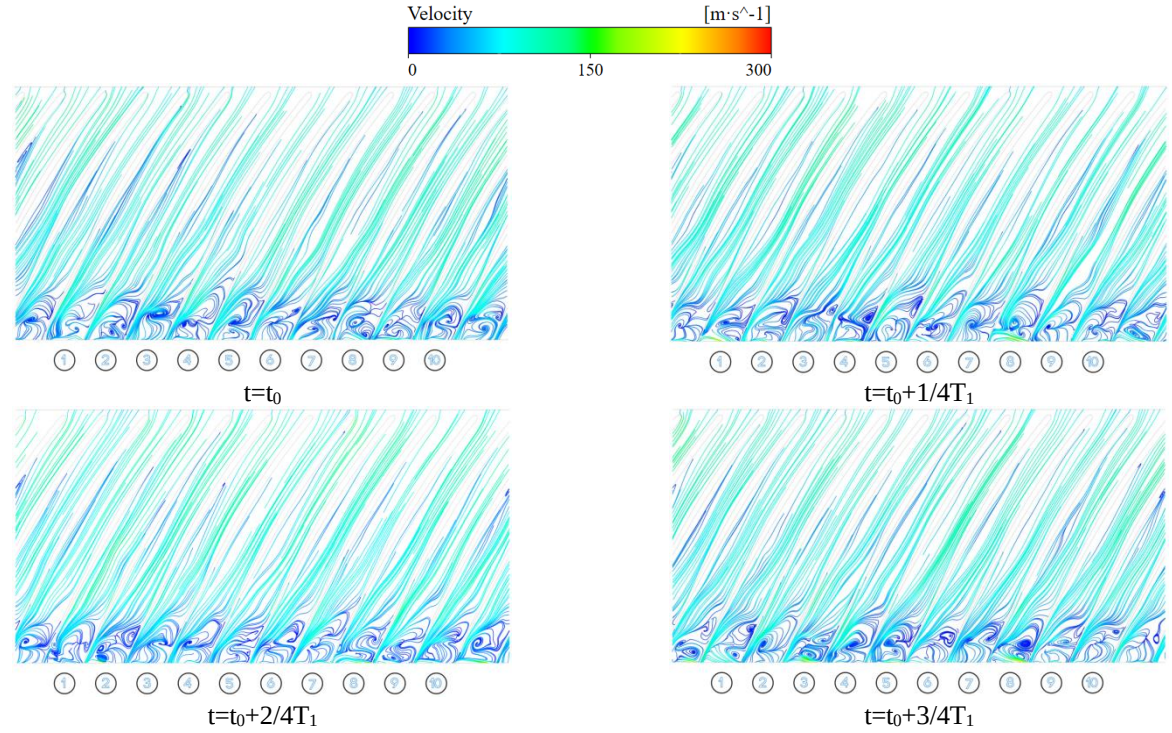

(b)

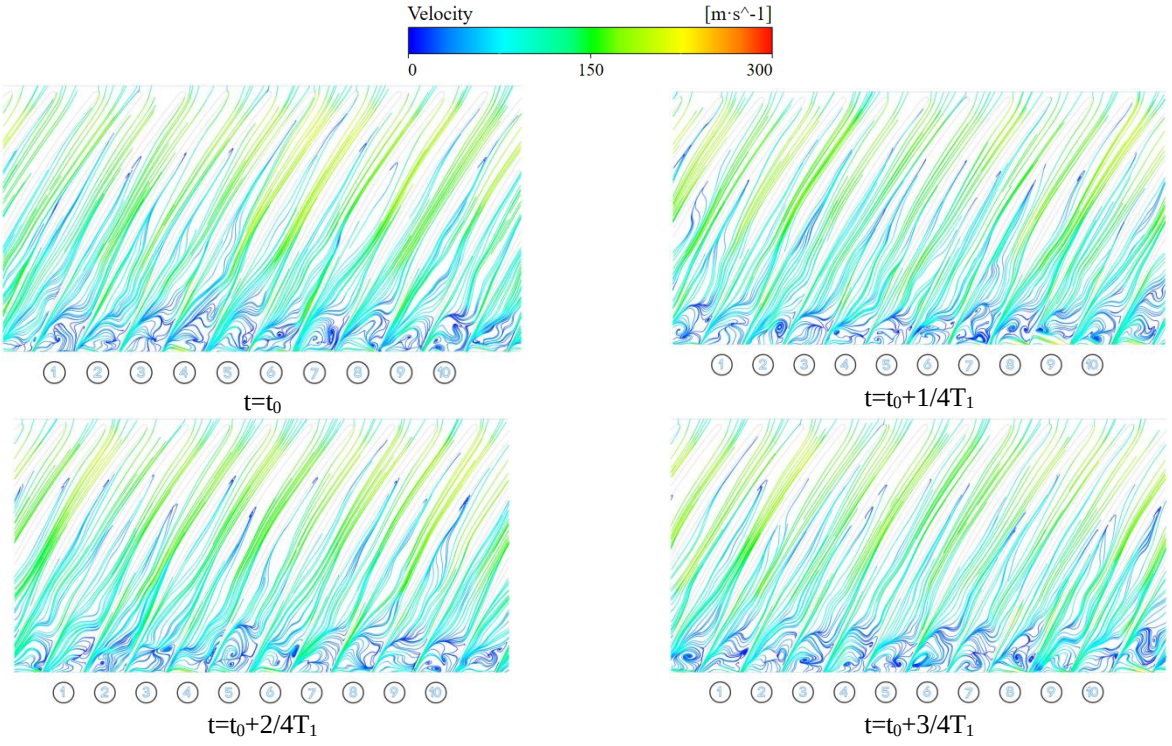

(c)

Fig. 13 Streamline patterns within a period on a 0.2 span at different conditions: (a) 0.7Q_d, (b) Q_d and (c) 1.4Q_d

Eventually, the two vortices gradually integrate and block the flow direction of the fluid again at time $t = t_0 + 3/4T_1$. The blockage propagates to channels 2 and 3 due to the increased flow inlet angle. The time-space evolution of the streamline is not completely consistent with that of each channel. A small vortex appears in channel 9 at t = t0; another vortex occurs in channel 9 at $t = t_0 + 1/4T_1$. These small vortices gradually develop and integrate into a big vortex at $t = t_0 + 1/2T_1$. A huge vortex can be detected in channel 9 at time $t = t_0 + 3/4T_1$. The temporal and spatial variation of flow can be compared intuitively through the transient streamlines, which can explore the blockage mechanism of this centrifugal blower in vacuum conditions.

Figure 13 (b) illustrates the time-space distribution of the streamline in a period in the design condition, and

no serious fluid blocking can be found. Channel 3 seriously blocked is selected as the target for analysis. A large vortex exists in channel 3 at t = t_0. The vortex has been separated, and the flow direction of the streamline has no obvious effect. The vortex area continuously decreases and the blockage gradually disappears at time t = t_0 + 1/2T_1. A big vortex generates in channel 3 at t = t_0 + 3/4T_1. Similarly, the blockage within passage 3 leads to the vortex propagating to adjacent passages. Vortices block the passage and the fluid cannot smoothly pass the flow channel, which seriously affects the performance of the centrifugal blower.

Figure 13(c) demonstrates the instantaneous streamline at 1.4Q_d within a rotating period. Channel 7 is chosen as the main focus while channel 8 should be concerned. Channel 7 is seriously blocked and the blockage of channel 8 is relatively slight at time t = t0. The vortex of channel 7 is separated into two vortices at t = t_0 + 1/4T_1, and a new vortex generates in channel 8. The vortex gradually disappears in channel 7 at t = t_0 + 1/2T_1. Vortices in channel 8 are integrated into a large vortex with time evolutions. The vortex in channel 7 has expanded again at t = t_0 + 3/4T_1, indicating that the vortex enters the second revolution. Meanwhile, the vortex of channel 8 reaches the maximum. The time-space evolution mentioned above indicates the blockage in a passage affects the adjacent passage. The streamlined evolution at different flow rates intuitively demonstrates the time-space characteristics of flow in the impeller. The blockage mechanism is studied to improve the centrifugal blower.

The Q-criterion is always used to study the dynamic characteristics and distribution of the separation vortex. Wang et al. (2018) numerically studied the generation of entropy in thermal convection with discrete boundary conditions at different Rayleigh numbers by the lattice-Boltzmann method. Xu et al. (2022) investigated the pressure and velocity fluctuations of tip-clearance flow in a compressor near stall. The Q-criterion is used to display the flow structure of the rotor field.

The Q-criterion equation is shown as follows:

$$\Omega_{ij} = \frac{1}{2}\left(\frac{\partial u_i}{\partial x_j} - \frac{\partial u_j}{\partial x_i}\right) \tag{11}$$

$$S_{ij} = \frac{1}{2}\left(\frac{\partial u_i}{\partial x_j} + \frac{\partial u_j}{\partial x_i}\right) \tag{12}$$

$$Q = \frac{1}{2}\left(\|\Omega\|^2 - \|S\|^2\right) \tag{13}$$

where Ω_{ij} is the vorticity tensor; S_{ij} is strain-rate tensor.

The physical mechanism of the positive Q value represents the region dominated by the vorticity and the negative value of the Q-criterion represents the area dominated by the strain rate or viscous stress. The iso-surface of the Q-criterion can precisely capture the vortex structure in the flow region and provide profound insight into the flow mechanism. Thus, the Q-criterion is used in the work to study the time-space characteristic of the vortex in vacuum.

Figure 14 displays the distribution of the vortices in the impeller within a period at different flow rates. The impeller rotates counterclockwise. The iso-surface of the Q-value that equals0.03 presents a distinct periodicity of vortex evolution after comparative analysis. Thus, the Q-criterion is selected as 0.03 to capture the subtle vortex evolution. Vortices are located at the impeller outlet. The shape is mainly performed as a wall-friction vortex near the pressure surface of the blade. Besides, vortices are generated near the red frame marked in Fig. 14.

Figure 14 (a) depicts the distribution of the vortex in the impeller within a rotating period at 0.7Q_d. A small vortex can be observed in the region marked by a red frame at t = t_0. The vortex area has increased and gradually move downstream at t = t_0 + 1/4T_1. The volume of the vortex expands again and moved obviously at t = t_0 + 1/2T_1. The vortex has disappeared completely at t = t_0 + 3/4T_1. One evolution cycle of vortices has been achieved at this stage and will enter the next stage

Figure 14 (b) describes the instantaneous vortex structure at four different moments within a rotating period, with the flow rate equal to the design condition. The vortex evolution is also captured and marked by the red frame. The captured vortex is weakened in the red frame at t_0, indicating that the flow structure is in moderation. The vortex region in the red frame significantly increases and the passage is blocked severely at t = t_0 + 1/4T_1. The vortex disappears at t = t_0 + 2/4T_1. Meanwhile, the vortex significantly increases in the next passage (on the left side of the red frame) because the blockage of the target passage in the previous moment increases the flow angle of the next passage and eventually leads to the blockage of the next channel. The vortex in the red frame disappears at t = t_0 + 3/4T_1, and a new vortex appears at the upper right corner of the marked frame. The onset of a new phase in the evolution of the vortex has commenced.

Compared with 0.7 Q_d, the area of the wall-friction vortex increases with the increased flow rate. The vortex-evolving period decreases with the increased flow rate. Besides, the blockage is caused due to the increased flow angle, and the flow structure of a passage can be influenced by a blockage in an adjacent passage. That is, the blockage of the flow path moves slowly in different flow paths.

Figure 14(c) shows the vortex structure at 1.4Q_d within a period. The region of the vortex increases with the increased flow rate. The fluid rolls and generates a vortex near the impeller inlet due to the changed fluid direction from axial to radial. The positive Q value indicates the area dominated by vorticity, and broken vortices are precisely captured through the Q-criterion. Vortices are mainly concentrated near the passage inlet, and large-scale wall friction vortices can be seen near the pressure surface of the blade. The rule of the vortex evolution at the flow rate is equal to that under design conditions. Flow in the passage marked at t_0 is stable

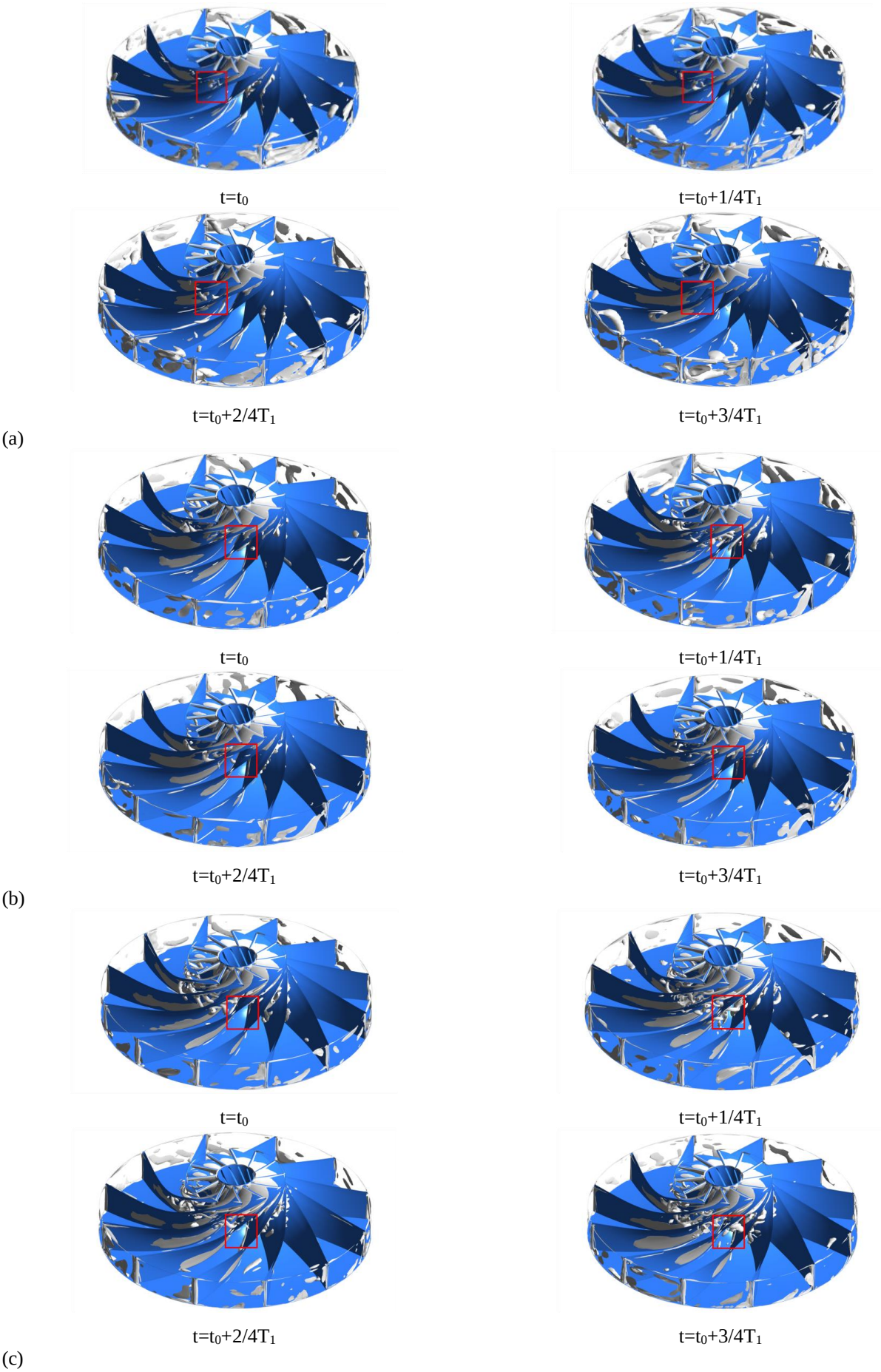

Fig. 14 Distribution of entropy in the impeller within one cycle at different conditions: (a) 0.7Q_d, (b) Q_d and (c) 1.4Q_d

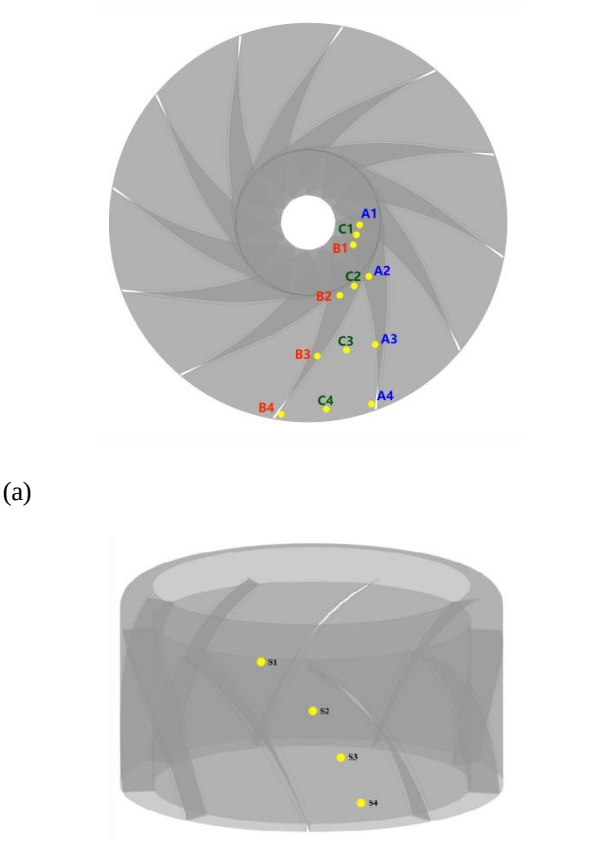

(a)

(b)

Fig. 15 Monitoring points in the (a) impeller and (b) flow diverter

with no vortex. Large-scale vortices are generated and block the passage at $t = t_0 + 1/4T_1$. These vortices disappear at $t = t_0 + 2/4T_1$, indicating one evolution cycle of vortices at this stage. However, the passage is blocked by vortices again at $t = t_0 + 3/4T_1$. The period of vortex evolution decreases significantly with increased mass flow, and the volume of vortices decreases near the impeller outlet by comparing different flow rates.

3.7 Pressure Fluctuations in Vacuum Conditions

As the above discussions, the time-space evolution of streamline and vortex structure distribution was displayed in the vacuum condition. The internal pressure fluctuations were analyzed in the impeller passage and flow diverter passage to reveal the spatio-temporal characteristic of the impeller in vacuum. Pressure fluctuation data for the first ten rotation cycles of the impeller were discarded due to the unstable internal pressure fluctuation of the impeller at the beginning of the rotation. The eleventh to twentieth rotating periods were chosen to analyze the pressure fluctuation. The pressure fluctuations within the flow passage were analyzed particularly through fast Fourier transform (FFT).

Figure 15 illustrates the monitoring points in the centrifugal blower and the flow diverter. The impeller in the figure rotates counterclockwise. Four monitoring points are uniformly arranged along the suction surface, pressure surface, and mid-passage to capture passage

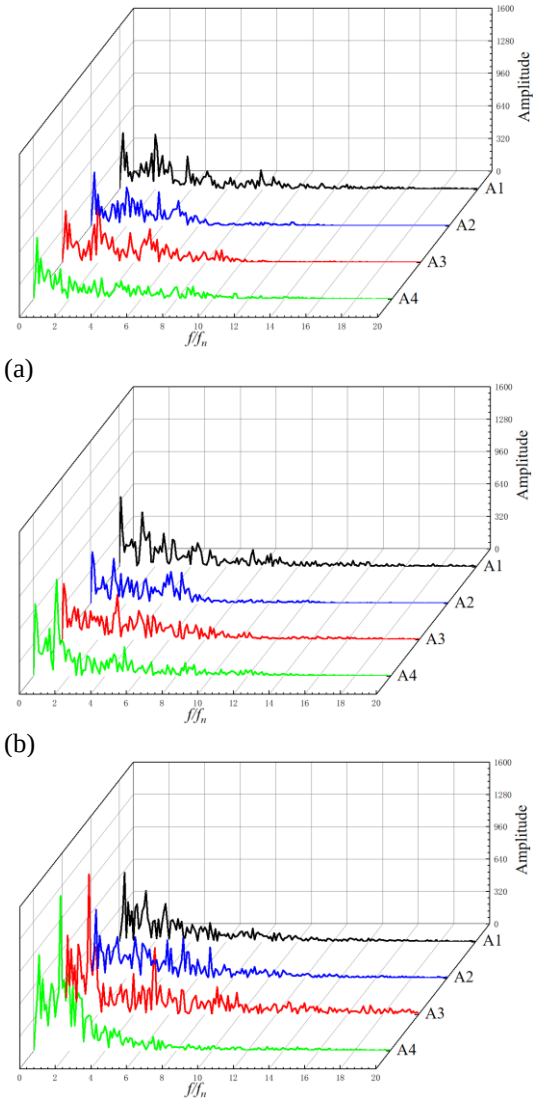

(a)

(b)

(c)

Fig. 16 Amplitude spectrum of each monitoring point along the suction surface of the blade at (a) 0.7Q_d, (b) Q_d and (c) 1.4Q_d

fluctuation characteristics near the 0.5 span of the impeller blade. Four monitoring points in the flow diverter are set evenly in the flow passage. The points near the suction surface of the blade are named A, the points near the pressure surface are named B, and the points located in the middle of the passage are named C (Fig. 15 (a)). The number of points is sequentially set from 1 to 4 along the passage. Figure 15 (b) presents the points in the flow diverter. The points in the passage are named S from 1 to 4 along the flow direction. Besides, the rotational speed of this impeller is 70,000rpm, and rotational frequency f_n is 1,166.67HZ.

Figure 16 presents the amplitude spectrum of each monitoring point near the suction surface of the impeller blade in various conditions. The abscissa is dimensionless by f_n. Figure 16(a) illustrates the pressure fluctuation of the monitoring points near the suction surface at 0.7Q_d. The amplitudes of each monitoring point have a series of slight disturbances, which originate from chaotic internal flow and serious flow separation in the vacuum condition. Pressure-fluctuation intensity at

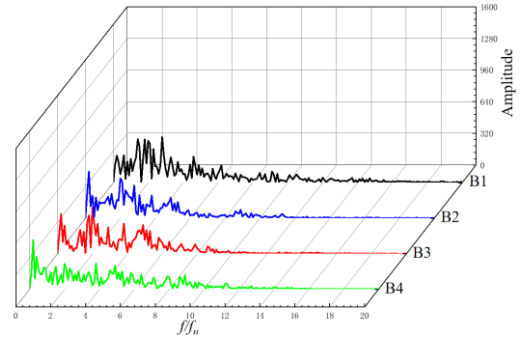

(a)

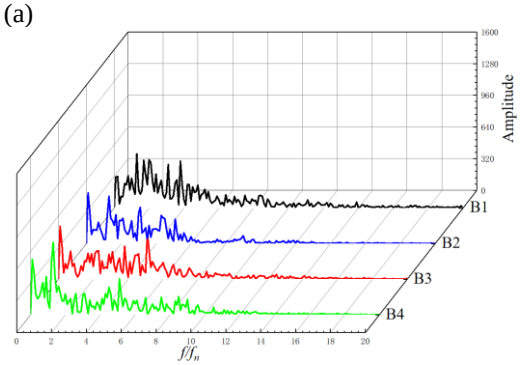

(b)

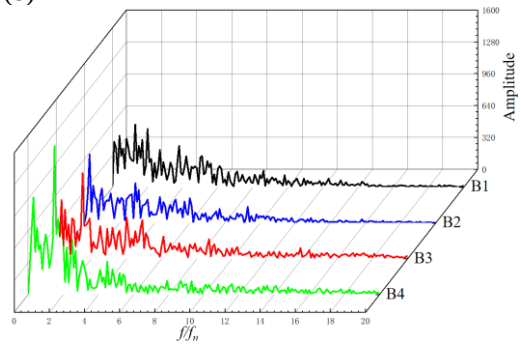

(c)

Fig. 17 Amplitude spectrum of each monitoring point along the pressure surface of the blade at (a) 0.7Q_d, (b) Q_d, and (c) 1.4Q_d

each point is close, and the frequency of the fluctuation peak is identical. The amplitudes of the first and second characteristic frequencies of each monitoring point increased with the increased flow rate in the Q_d working condition (Fig. 16 (b)), especially on the monitoring point near the outlet of the impeller passage.

Figure 16 (c) shows the amplitude spectrum at a mass flow rate equal to 1.4 Q_d. The fluctuations of the first and second characteristics are captured at monitoring points A3 and A4. Their fluctuations near the impeller outlet significantly increase. The intensity of the flow interaction inside this impeller becomes increasingly severe with increased flow. The soar of pressure fluctuations at point A3 indicates that the disturbance area of separation flow is gradually expanding towards the upstream flow passage with increased flow. The pressure fluctuation within the impeller is composed of disturbances caused by fluid separation and becomes more severe as the flow rate increases in vacuum. The fluid mechanism in near vacuum (extremely low flow rate) is different from that at a low flow rate.

Figure 17 describes the pressure fluctuation at the monitoring points near the pressure surface of the blade in different working conditions. Compared to the pressure fluctuation near the suction surface of the blade, the amplitude of pressure fluctuations near the blade pressure surface is increasingly enhanced. The turbulent structure near the blade suction surface is more complex. Figure 17 (a) shows the amplitude spectra of each monitoring point at 0.7 Q_d. The pressure fluctuation at each monitoring point is similar to the pattern near the suction surface. The amplitudes of pressure fluctuations in the whole passage remain at the same level. The amplitude of pressure fluctuation appears at a peak at point B4, and the pressure fluctuation on the other monitoring points has no obvious change in the design condition (Fig. 17 (b)). The pressure fluctuation amplitudes of each point are generally more serious at a flow rate of 1.4 Qd than that of the design condition, especially reflected on points B3 and B4. The sharp increase of pressure fluctuations near the blade pressure surface is well consistent with the phenomenon near the suction surface.

Compared to the region near the blade, the middle of the passage is the more stable area. Therefore, Fig. 18 shows the amplitude spectra of monitoring points in the middle of the passage. The amplitude spectra of monitoring points in the middle of the passage are similar to the pressure fluctuation near the blade, and the amplitude gradually increases with the increased flow rate. The pressure fluctuations near the impeller outlet are still more sensitive to changes in the flow rate. Besides, a large amplitude component can be found as the frequency is equal to a rotational frequency of 0.1. The flow region is chaotic, and the flow separation severely occurs, with the stall mass seriously blocked.

Generally, the pressure fluctuation near the impeller outlet represents a significant way to understand stall at a low flow rate. Figures 16-18 show that the pressure fluctuation near the impeller outlet is the most sensitive to the variation of the flow rate. Therefore, Fig. 19 presents the pressure fluctuation near the trailing edge of the suction surface (A4) and pressure surface (B4) and that near the outlet of the middle of the passage (C4) under design conditions. The abscissa is nondimensionalized by a rotational frequency. Regardless of whether the monitoring point is located on the pressure surface, suction surface, or in the middle of the channel, the characteristic frequency is identical. The first characteristic frequency is 1.3 f_n, and the second and the third characteristic frequencies are 0.1 and 5.1f_n, respectively. The first and third characteristic frequencies are both within the super synchronous frequency range ($f/f_n > 1$), indicating the blade passage frequency is caused by the dynamic and static interference between the impeller and flow diverter. The second characteristic frequency is inside the subsynchronous frequency range ($f/f_n < 1$) induced by the flow-instability phenomenon like flow separation and vortex shedding. Besides, low-frequency fluctuation

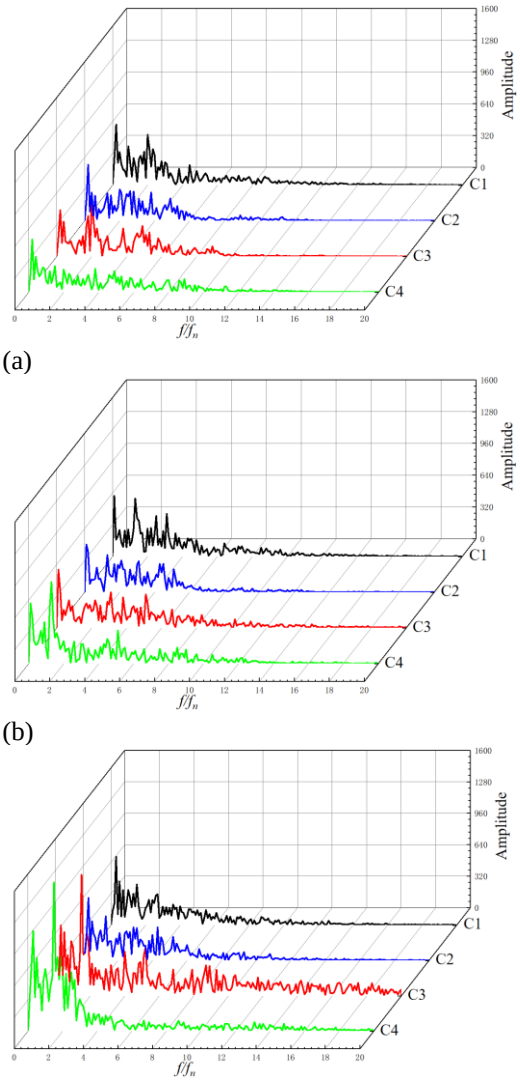

Fig. 18 Amplitude spectrum of each monitoring point along the middle of passage at: (a) 0.7Q_d, (b) Q_d, and (c) 1.4Q_d

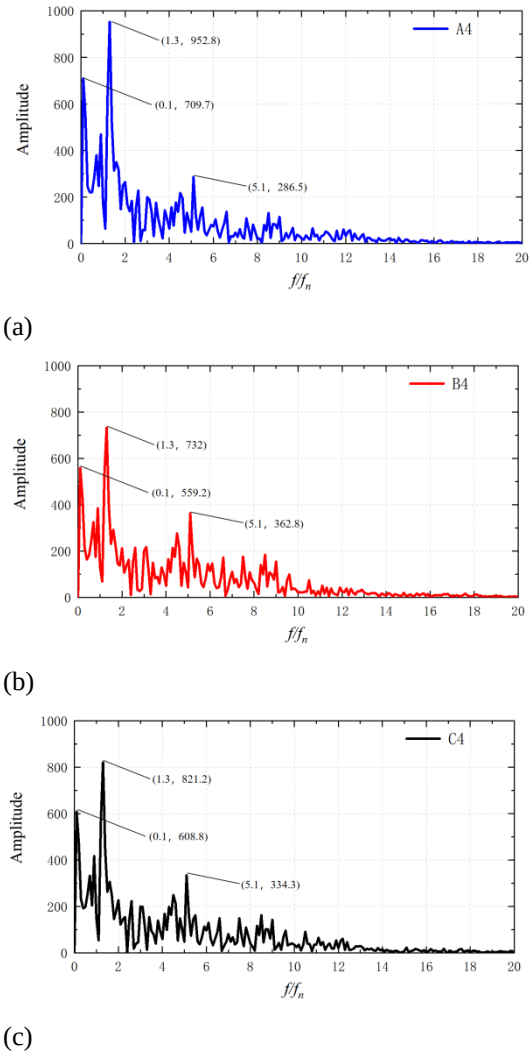

Fig. 19 Amplitude spectrum of monitoring point (a) A4, (b)B4, and (c) C4 at Qd

intensity is greater near the blade suction surface, while there is a stronger high-frequency disturbance near the pressure surface of the blade. The fluctuation at monitoring point C4 falls somewhere between the two.

Figure 20 illustrates the amplitude spectra of monitoring points along the flow diverter passage in three working conditions. The fluctuation peaks mainly concentrate at the inlet of the diverter passage. The general law of pressure-fluctuation distribution in the flow diverter can be obtained, that is, the pressure fluctuation reaches a maximum at the inlet of the flow diverter and decreases continuously along the passage. The fluid reaching the flow diverter has huge kinetic energy due to the high-speed impeller, and only energy losses exist in the flow process within the flow diverter. Besides, the pressure fluctuations of each point gradually increaseas the flow rate increases, which is consistent with the phenomenon in the impeller.

Finally, the physical mechanism of the centrifugal blower suction system in vacuum is revealed preliminarily by numerical results. The suction system mainly used in vacuum cleaners has low efficiency due to the pursuit of high vacuum. It is easy to affect or damage other parts (like the motor) of the centrifugal blower when the flow passage is seriously blocked. The physical insight of the work is studied to explore the temporal-spatial characteristics of the blockage mechanism of this system based on the working state of this system in vacuum. The profile of the impeller blade will be optimized to improve the vacuum degree and working of the system in the future.

4. CONCLUSIONS

The 3D impeller suction system in vacuum conditions was investigated by numerical simulations. Some conclusions were presented as follows.

(1) The efficiency and vacuum degree with different flow rates of the centrifugal blower were demonstrated by numerical simulations, which laid a foundation to improve the blower vacuum.

(2) The steady-state characteristics of this centrifugal blower at three different low flow were analyzed more precisely with the pressure, temperature,

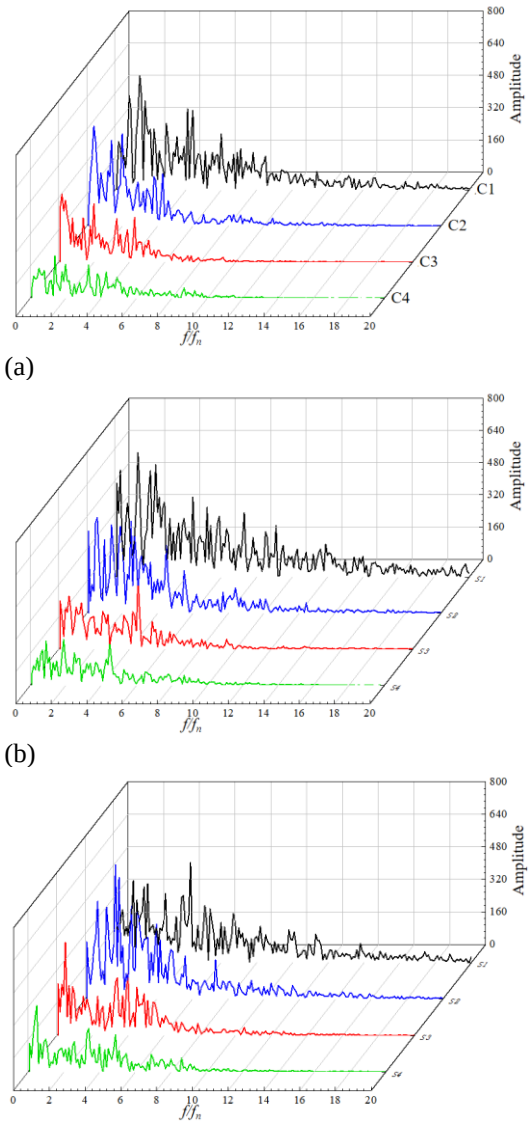

(a) (b) (c)

Fig. 20 Amplitude spectrum of each monitoring point along the flow diverter passage at (a) 0.7Q_d, (b) Q_d, and (c) 1.4Q_d

and streamline diagram. The numerical results indicated that the fluid backflow was obvious in the vacuum working conditions. Vortices with large scales were generated with the decreased flow rate in the passage region. The working mechanism of the centrifugal blower was further explained by the distribution of backflow and vortices in detail.

(3) The blockage mechanism of fluid inside the impeller was visually reflected through the time-space evolution of the streamline. The generation, propagation and extinction processes of vortices have been elaborately exhibited in this work. The evolution of vortices could explain the energy loss inside the centrifugal blower and analyze the energy losses inside the centrifugal blower.

(4) The analysis of pressure fluctuation and frequency spectrum based on the FFT transform indicated that the pressure fluctuation in the three-dimension passage of the impeller was mainly composed of the pressure fluctuation due to rotating stall and flow separation. The shaft frequency was difficult to identify because of flow disturbances. The pressure fluctuation became more violent as the flow rate increased in vacuum conditions.

AUTHORS CONTRIBUTION

Writing—Original Draft Preparation, Y. Li; Data Curation, B. Zhang; Review & Editing, Y. Chen; Modifications of Language, Z. Wang; Modifications of Figures, H. Yang; Project Administration, Y. Wei. All authors have read and agreed to the published version of the manuscript.

ACKNOWLEDGMENTS

This work was supported by the National Natural Science Foundation of China (GrantNo.U22A20589), Natural Science Foundation Key Projects of Zhejiang Province (Grant No. LZ22E060002), the Science and Technology Plan Project of Zhejiang Province (Grant No. LGG21E060003), and the Science and Technology Key Plan Project of Zhejiang Province (Grant No. 2021C01049 and 2020C04011).

CONFLICTS OF INTEREST

The authors declare there are no known conflicts of interest associated with this publication and there has been no significant financial support for this work that could have influenced its outcome. We confirm that the paper has been read and approved by all named authors and that there are no other persons who satisfied the criteria for authorship but are not listed.

REFERENCES

An, K., Kwon, H., & J. Jang (2022). Acoustic metamaterial design for noise reduction in vacuum cleaner. *Journal of Mechanical Science and Technology*, 36(11), 5353-5362. https://doi.org/10.1007/s12206-022-1002-0

Borello, D., A. Corsini, G. Delibra, M. Fiorito (2013). Large-eddy simulation of a tunnel ventilation fan. *Journal of Fluids Engineering*, 135(7), 071102, 1-9. https://doi.org/10.1115/1.4023686

Cao, Z., Zhang, X., & Y. Liang (2022). Influence of blade lean on performance and shock wave/tip leakage flow interaction in a transonic compressor rotor. *Journal of Applied Fluid Mechanics*, 15(1), 153-167. https://doi.org/10.47176/jafm.15.01.32753

Chen, Y., Wang, Z., & Yang, H. (2023). Spatiotemporal characteristics and pressure fluctuations of internal flow in a high-speed centrifugal blower for vacuum cleaner at low flow-rate conditions. *Journal of Applied Fluid Mechanics*, 16(2), 375-388. https://doi.org/10.47176/jafm.16.02.1245

Dang, Z., Zhang, Z., & Gao, M. (2019). Numerical simulation of thermal performance for super large-scale wet cooling tower equipped with an axial fan.

International Journal of Heat and Mass Transfer. 135, 220-234. https://doi.org/10.1016/j.ijheatmasstransfer.2019.01.111

Du, Y., Dou, H., F. Lu (2020). Counter-propagation stall of vaned diffuser in a centrifugal compressor near design condition. *Journal of Turbomachinery*, 142(11). https://doi.org/10.1115/1.4048604

Ghenaiet, A., & Khalfallah, S. (2019). Assessment of some stall-onset criteria for compressor compressors. *Aerospace Science and Technology*, 88, 193-207. https://doi.org/10.1016/j.ast.2018.12.039

He, X., & Zheng, X. (2016). Mechanisms of lean on the performance of transonic centrifugal compressor impellers. *Journal of Propul Power*, 32(5), 1220-1229. https://doi.org/10.2514/1.B36008

Jeon, W., Baek, S., & Kim, C. (2003). Analysis of the aeroacoustic characteristics of the centrifugal fan in a vacuum cleaner. *Journal of Sound and Vibration*, 268(5), 1025-1035. https://doi.org/10.1016/s0022-460x(03)00319-5

Li, Z., Lu, X., & Zhang, Y. (2018). Numerical investigation of a highly loaded centrifugal compressor stage with a tandem bladed impeller. *Proceedings of the Institution of Mechanical Engineers Part A Journal of Power and Energy*, 232(3), 240-253. https://doi.org/10.1177/0957650917725406

Liu, X., Li, Y., & Liu, Z. (2022). Experimental and numerical investigation of stall mechanism in centrifugal pump impeller. *Journal of Applied Fluid Mechanics*. 15(3), 927-641. https://doi.org/10.47176/jafm.15.03.33165

Mischo, B., Jenny, P., & Mauri, S. (2018). Numerical and experimental fluid-structure interaction-study to determine mechanical stresses induced by rotating stall in unshrouded centrifugal compressor impellers. *Journal of Turbomachinery*, 140(11). https://doi.org/10.1115/1.4041400

Niu, Z., Sun, Z., & Wang, B. (2022). Effects of nonaxisymmetic volute on rotating stall in the vaneless diffuser of centrifugal compressors. *Journal of Engineering for Gas Turbines and Power*, 144(5). https://doi.org/10.1115/1.4053389

Semlitsch, B., & M. Mihăescu (2016). Flow phenomena leading to surge in a centrifugal compressor. *Energy*, 103, 572-587. https://doi.org/10.1016/j.energy.2016.03.032

Soheil, A., & Mahdi, G. M. (2022). Optimization of a vacuum cleaner fan suction and shaft power using Kriging surrogate model and MIGA. *Proceedings of the Institution of Mechanical Engineers, Part A: Journal of Power*, 236(3), 519-537. https://doi.org/10.1177/09576509211049613

Vad, J. (2008). Aerodynamic effects of blade sweep and skew in low-speed axial flow rotors at the design flow rate: an overview. *Proceedings of the Institution of Mechanical Engineers Part A Journal of Power and Energy*, 222(1), 69-85. https://doi.org/10.1243/09576509JPE471

Wang, Z., Wei, Y., & Qian Y. (2018). Numerical study on entropy generation in thermal convection with differentially discrete heat boundary conditions. *Entropy*, 20(5), 351. https://doi.org/10.3390/e20050351

Wang, Z., Wei, Y. & Qian Y. (2020). A bounce back-immersed boundary-lattice Boltzmann model for curved boundary. *Applied Mathematical Modelling*, 81, 428-440. https://doi.org/10.1016/j.apm.2020.01.012

Wei, Y., Zhu, L. & Wang, Z. (2020). Numerical and experimental investigations on the flow and noise characteristics in a centrifugal fan with step tongue volutes. *Proceedings of the Institution of Mechanical Engineers Part C Journal of Mechanical Engineering Science*, 234(15), 2979-2993. https://doi.org/10.1177/0954406219890920

Wolfram, D., & Carolus, T. H. (2010). Experimental and numerical investigation of the unsteady flow field and tone generation in an isolated centrifugal fan impeller. *Journal of Sound & Vibration*, 329(21), 4380-4397. https://doi.org/10.1016/j.jsv.2010.04.034

Xue, X., & Wang, T. (2019). Stall recognition for centrifugal compressors during speed transients. *Applied Thermal Engineering*, 153, 104-112. https://doi.org/10.1016/j.applthermaleng.2019.02.027

Yuki, A., Yoshifumi, Y. & Nobumichi, F. (2022). Behavior of vaneless diffuser stall in a centrifugal compressor. *Journal of Thermal Science*, 31(1), 3-12. https://doi.org/10.1007/s11630-022-1557-1

Zhang, L., He, R., & Wang, S. (2020). A review of rotating stall in vaneless diffuser of centrifugal compressor. *Journal of Thermal Science*, 29(1), 323-342. https://doi.org/10.1007/s11630-020-1261-y

Zhang, H., Yang, C., & Shi, X. (2021a). Two stall stages in a centrifugal compressor with a vaneless diffuser.*Aerospace Science and Technology*, 110. https://doi.org/10.1016/j.ast.2021.106496

Zhang, Y., Lu, X., & Zhang Y. (2021b). Stall behavior in an ultra-high-pressure-ratio centrifugal compressor: backward-traveling rotating stall. *Journal of Turbomachinery*, 1-51. https://doi.org/10.1115/1.4050918